

GPU-based visualization of domain-coloured algebraic Riemann surfaces

Stefan Kranich*

11 November 2015

Abstract

We examine an algorithm for the visualization of domain-coloured Riemann surfaces of plane algebraic curves. The approach faithfully reproduces the topology and the holomorphic structure of the Riemann surface. We discuss how the algorithm can be implemented efficiently in OpenGL with geometry shaders, and (less efficiently) even in WebGL with multiple render targets and floating point textures. While the generation of the surface takes noticeable time in both implementations, the visualization of a cached Riemann surface mesh is possible with interactive performance. This allows us to visually explore otherwise almost unimaginable mathematical objects. As examples, we look at the complex square root and the folium of Descartes. For the folium of Descartes, the visualization reveals features of the algebraic curve that are not obvious from its equation.

1 Introduction

1.1 Mathematical background

The following basic example illustrates what we would like to visualize.

Example 1.1. Let y be the square root of x ,

$$y = \sqrt{x}.$$

If x is a non-negative real number, we typically define y as the non-negative real number whose square equals x , i.e. we always choose the non-negative solution of the equation

$$y^2 - x = 0 \tag{1}$$

as $y = \sqrt{x}$. For negative real numbers x , no real number y solves Equation 1. However, if we define the imaginary unit i as a number with the property that $i^2 = -1$ then the square root of x becomes the purely imaginary number

$$y = i\sqrt{|x|}.$$

*Zentrum Mathematik (M10), Technische Universität München, 85747 Garching, Germany; E-mail address: kranich@ma.tum.de

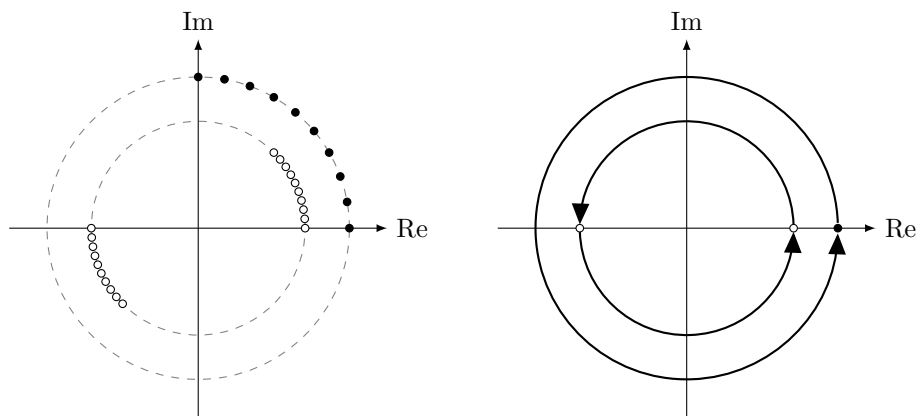


Figure 1.2: When a complex number (black points) runs along a circle centred at the origin of the complex plane, its square roots (white points) move at half the angular velocity (left image). After a full turn of x , the square roots have interchanged positions. The real part of the square root that initially had positive real part has become negative, and vice versa (right image).

Together, these two conventions yield a continuous square root function

$$\sqrt{\cdot}: \mathbb{R} \rightarrow \mathbb{C}.$$

For complex numbers x , Equation 1 has exactly two complex solutions (counted with multiplicity), the square roots of x .

We have seen that, for real numbers x , we can choose one solution of Equation 1 for the square root and obtain a square root function that is continuous over the real numbers. In contrast, we cannot for every complex number x choose one solution of Equation 1 so that we obtain a square root function that is continuous over the complex numbers: If we plot the two solutions of Equation 1 as x runs along a circle centred at the origin of the complex plane, we observe that y moves at half the angular velocity of x (see Figure 1.2). When x completes one full circle and reaches its initial position again, the square roots have interchanged signs. Therefore, a discontinuity occurs when x returns to its initial position after one full turn and the square root jumps back to its initial position.

Note that by choosing the values of the square root in a different manner, or, equivalently, letting x start at a different position, we can move the discontinuity to an arbitrary position on the circle. Moreover, note that there is (at least) one discontinuity on any circle of any radius centred at the origin.

In order to define the principal branch of the complex square root function, we usually align the discontinuities along the negative real axis, the canonical branch cut of the complex square root function, and choose those values that on the real axis agree with the square root over the real numbers.

Alternatively, we can extend the domain of the complex square root to make it a single-valued and continuous function. To that end, we take two copies of

the extended complex plane and slit them along the negative real axis. On the first copy, we choose the solution of Equation 1 with non-negative real part as the complex square root of x ; on the second copy, we choose the other solution. We glue the upper side (lower side) of the slit of the first copy to the lower side (upper side) of the slit of the second copy and obtain a Riemann surface of the complex square root. (In three dimensions, this is not possible without self-intersections.)

Remark 1.3. On the Riemann surface, the complex square root is single-valued and continuous. It is even analytic except at the origin and at infinity, which are exactly the points where the two solutions of Equation 1 coincide.

Remark 1.4. The branch cut is not a special curve of the Riemann surface. When we glue the Riemann surface together, the branch cut becomes a curve like every other curve on the Riemann surface. If we had used a different curve between the origin and infinity as branch cut, we would have obtained the same result.

Remark 1.5. Equation 1 describes a parabola. We can proceed analogously to obtain Riemann surfaces for other plane algebraic curves.

1.2 Previous work

Probably the most common approach for visualization of functions is to plot a function graph. However, for a complex function

$$g: \mathbb{C} \rightarrow \mathbb{C},$$

the function graph

$$\{(z, g(z)) \mid z \in \mathbb{C}\} \subset \mathbb{C} \times \mathbb{C} \simeq \mathbb{R}^2 \times \mathbb{R}^2$$

is a (real) two-dimensional surface in (real) four-dimensional space.

One way to visualize a four-dimensional object is to plot several two- or three-dimensional slices. This approach seems less useful for understanding the overall structure of the object.

Another traditional method to visualize complex functions is domain colouring. The principle of domain colouring is to colour every point in the domain of a function with the colour of its function value in a reference image. If we choose the reference image wisely, a lot of information about the complex function can be read off from the resulting two-dimensional image (see e.g. (Poelke and Polthier, 2012) and (Wegert, 2012)). The idea of lifting domain colouring to Riemann surfaces is due to Poelke and Polthier (2009).

We can interpret a Riemann surface of a plane algebraic curve

$$\mathcal{C}: f(x, y) = 0 \tag{2}$$

as a function graph of a multivalued complex function, which maps every x to multiple values of y . If $f(x, y)$ is a polynomial of degree n in y , there are exactly n values of y for every value of x that satisfy $f(x, y) = 0$ (counted with

multiplicity). Every such pair (x, y) corresponds to a point on the Riemann surface. In other words, the Riemann surface is an n -fold cover of the complex plane.

Let $\pi: (x, y) \mapsto x$ denote a projection function on the Riemann surface. Then the values of y at x correspond to the elements of the fibre $\pi^{-1}(x)$. The situation is analogous to function graphs of single-valued functions from the real numbers (or the real plane) to the real numbers, where one function value lies above every point in the domain.

We can transfer the Riemann surface from (real) four-dimensional space into (real) three-dimensional space by introducing a height function $H: \mathbb{C} \rightarrow \mathbb{R}$. We typically use the real part as a height function. We plot the surface

$$\{(\operatorname{Re} x, \operatorname{Im} x, H(y)) \mid x, y \in \mathbb{C}: f(x, y) = 0\}$$

and use domain colouring to represent the value of y at every point of the surface.

In practice, we want to generate a triangle mesh that approximates the Riemann surface as the graph of a multivalued function over a triangulated domain in the complex plane. The Riemann surface mesh approximates the continuous Riemann surface in the following sense: The y -values at the vertices of a triangle of the Riemann surface mesh result from each other under analytic continuation along the edges of the underlying triangle in the triangulated domain. If $f(x, y) = 0$ is a polynomial of degree n in y there are n values of y above every vertex x of the triangulated domain. Hence, we have to determine which of the $3n$ values of y above a triangle in the triangulated domain form triangles of the Riemann surface mesh. A wrong combination of values of y to triangles might for example occur due to discontinuity if we used the principal branch of the square root function for the computation of y . This would produce artefacts in the visualization for which there is no mathematical justification.

For the generation of such a Riemann surface mesh, previous algorithms have solved systems of differential equations (Trott, 2008; Nieser et al., 2010) or explicitly identified and analyzed branch cuts to remove discontinuities (Kranich, 2012; Wegert, 2012, Section 7.6).

In the next section, we discuss an algorithm based on a different idea: We can exploit that $y(x)$ is continuous almost everywhere on the Riemann surface and therefore, if x changes little, so does $y(x)$.

2 Algorithms

In this section, we describe algorithms for generating and visualizing domain-coloured Riemann surface meshes of plane algebraic curves. Let

$$\mathcal{C}: f(x, y) = 0 \tag{3}$$

be a complex plane algebraic curve. In particular, let f be a polynomial with complex coefficients of degree n in y . Moreover let $U \subset \mathbb{C}$ be a triangulated domain in the complex plane. (In practice, U is typically rectangular.)

We want to generate a Riemann surface mesh of \mathcal{C} . The mesh discretizes a part of a (real) two-dimensional surface in (real) four-dimensional space. We can visualize it using a height function and domain colouring, as described in the previous section.

We obtain a Riemann surface mesh of \mathcal{C} as a graph of the multivalued function induced by Equation 3, which maps every value of x in U to n values of y such that $f(x, y) = 0$.

For every triangle in U , we thus obtain n values of y at each of its three vertices. The problem is to determine whether, and if so, how, the $3n$ values of y can be combined to form triangles of the Riemann surface mesh. The resulting triangles should be consistent with the fact that y as a function of x is analytic almost everywhere on the Riemann surface. This is impossible if the triangle in U contains a ramification point of $y(x)$. In this case, we subdivide the triangle to obtain smaller triangles mostly free of ramification points. Otherwise, the triangles of the Riemann surface mesh are uniquely determined by analytic continuation of $y(x)$ along the edges of the triangle in U .

In order to find these triangles of the Riemann surface mesh, we use the following idea: Consider a triangle $\Delta x_1 x_2 x_3$ in U that is free of ramification points of $y(x)$. Under this assumption, $y(x)$ is continuous on those parts of the Riemann surface that lie above $\Delta x_1 x_2 x_3$. Hence, for every $\varepsilon > 0$ there exists $\delta > 0$ such that $|y(x_1) - y(x_2)| < \varepsilon$ for all x_1, x_2 with $|x_1 - x_2| < \delta$. If ε is half the minimum distance between the n values of $y(x)$ at x_1 and $|x_1 - x_2|$ is smaller than the corresponding δ , then the values of $y(x)$ at x_2 are closer to the corresponding values of $y(x)$ at x_1 than to any other value of $y(x)$ at x_1 .

In other words, if triangle $\Delta x_1 x_2 x_3$ is small enough, we can combine the values of y at its vertices to triangles of the Riemann surface mesh based on proximity: Among the $3n$ values of y at the vertices of triangle $\Delta x_1 x_2 x_3$, every three values of y closest to each other form a triangle of the Riemann surface mesh.

We can algorithmically compute a $\delta > 0$ as above using the epsilon-delta bound for plane algebraic curves of Theorem 3.1. Theorem 3.1 is of essential importance for our approach. Our approach only works because Theorem 3.1 provides us with a reliable bound computable as a function of x that depends only on a few constants derived from the coefficients of $f(x, y)$.

If triangle $\Delta x_1 x_2 x_3$ is not small enough to correctly combine the values of y at its vertices based on proximity, we subdivide the triangle.

In summary, we obtain the following algorithm:

Algorithm 2.1 (Generation of a Riemann surface mesh). Let $U \subset \mathbb{C}$ be a triangulated domain in the complex plane. Let

$$\mathcal{C}: f(x, y) = 0$$

be a complex plane algebraic curve and $f(x, y)$ a polynomial of degree n in y . We prescribe a maximal subdivision depth (as a maximal number of iterations or as a minimal edge length).

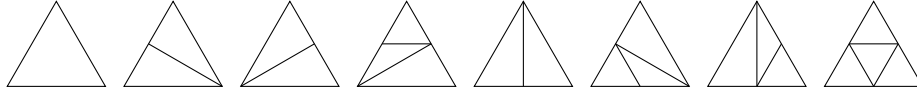


Figure 2.2: Adaptive refinement patterns used in Algorithm 2.1

1. Compute the global ingredients of the epsilon-delta bound of Theorem 3.1 for $y(x)$.
2. For every triangle $\Delta x_1 x_2 x_3$ in U :
 - (a) Compute the $3n$ values of $y(x)$ at x_1, x_2, x_3 ,

$$\{y_k(x_j) \mid f(x_j, y_k(x_j)) = 0, j = 1, 2, 3, k = 1, 2, \dots, n\}.$$

- (b) Compute half the minimum distance between the values of $y(x)$ at each of the vertices of $\Delta x_1 x_2 x_3$,

$$\varepsilon(x_j) = \frac{1}{2} \min_{k \neq l} |y_k(x_j) - y_l(x_j)|, \quad j = 1, 2, 3.$$

- (c) Compute $\delta(x_j)$ by the epsilon-delta bound of Theorem 3.1 so that

$$|y(x_j) - y(x)| < \varepsilon(x_j), \text{ if } |x_j - x| < \delta(x_j), \quad j = 1, 2, 3.$$

- (d) Determine which of the edges of $\Delta x_1 x_2 x_3$ are longer than the minimum of the $\delta(x_j)$ at their endpoints and must be subdivided.
- (e) Select the right adaptive refinement pattern (see Figure 2.2) and subdivide $\Delta x_1 x_2 x_3$ accordingly.

3. Repeat step 2 until the maximal subdivision depth is reached.
4. Discard every triangle in U with an edge longer than the minimum of the $\delta(x_j)$ at its endpoints.
5. For every triangle $\Delta x_1 x_2 x_3$ in U , combine the values of $y(x)$ at its vertices to triangles of the Riemann surface mesh based on proximity. More formally, the triangles added to the Riemann surface mesh comprise the vertices

$$\begin{aligned} & (x_1, y_k(x_1)), \\ & (x_2, \operatorname{argmin}_{y_l(x_2)} |y_k(x_1) - y_l(x_2)|), \\ & (x_3, \operatorname{argmin}_{y_l(x_3)} |y_k(x_1) - y_l(x_3)|), \end{aligned}$$

for $k = 1, 2, \dots, n$.

6. Output the Riemann surface mesh and stop.

Remark 2.3. By construction, Algorithm 2.1 generates a Riemann surface mesh that is consistent with the analytic structure of the Riemann surface of \mathcal{C} .

Remark 2.4. The adaptive refinement patterns used for the subdivision of triangles, whose edges are too long, produce a watertight subdivision.

Remark 2.5. Step 4 of Algorithm 2.1 produces holes around the ramification points of $y(x)$. We can make these holes very small if we choose the maximal subdivision depth appropriately.

For the visualization of a Riemann surface mesh, we use the following algorithm:

Algorithm 2.6 (Visualization of a Riemann surface mesh). Let a Riemann surface mesh and a domain colouring reference image be given. We choose a height function $H: \mathbb{C} \rightarrow \mathbb{R}$ to transform a point on the Riemann surface mesh from (real) four-dimensional space to a point in (real) three-dimensional space,

$$(x, y(x)) \mapsto (\operatorname{Re} x, \operatorname{Im} x, H(y(x))).$$

1. Draw the mesh that results from transforming every vertex of the Riemann surface mesh as above.
2. Interpolate the value of $y(x)$ on the transformed mesh.
3. Assign to every point on the transformed mesh the colour in the reference image of the value that $y(x)$ attains at that point on the transformed mesh.

Remark 2.7. If we choose the real (or imaginary) part of $y(x)$ as a height function, the transformation from (real) four-dimensional to (real) three-dimensional space becomes a projection.

Remark 2.8. Using the real part of $y(x)$ as a height function has the advantage that the visualization then contains the image of \mathcal{C} interpreted as a real plane algebraic curve. It is the intersection of the visualization of the Riemann surface mesh in (real) three-dimensional space with the $\operatorname{Re} x$ - $\operatorname{Re} y$ -plane (the xz -plane, if we label the coordinate axes of real three-dimensional space such that the x -axis points to the right and the z -axis points upwards).

Remark 2.9. The computation of the Riemann surface mesh by Algorithm 2.1 is independent of the choice of height function used for its visualization.

3 Implementation

In this section, we discuss how Algorithm 2.1 and Algorithm 2.6 can be implemented using OpenGL and WebGL. Since WebGL targets a much wider range of devices, its API is more limited than that of OpenGL. Consequently, our implementation using WebGL differs substantially from our implementation using OpenGL. Before we discuss each setup separately, let us talk about what they have in common.

The main part of our programs is written in shading language (GLSL for OpenGL and ESSL for WebGL) and runs on the GPU. We use the CPU to

compute the global ingredients for the epsilon-delta bound, to generate shading language code that computes the epsilon-delta bound for $\mathcal{C}: f(x, y) = 0$ as a function of x , and to generate a coarse triangulation of the input domain.

The implementations in OpenGL and WebGL share some shading language code. Since there is no native type for complex numbers, we represent them using two-dimensional floating point vectors. Common routines include complex arithmetic, numerical root-finding algorithms, the computation of the epsilon-delta bound, and domain colouring.

The implementation of complex arithmetic is straightforward and we shall not go into detail about it.

We need numerical root-finding algorithms to approximate roots of polynomials in order to compute values of $y(x)$ (and to compute the global ingredients of the epsilon-delta bound). For instance, Laguerre's method (Press et al., 2007, Section 9.5.1) and deflation (Press et al., 2007, Section 9.5.3) or Weierstraß–Durand–Kerner method (Weierstraß, 1891; Durand, 1960; Kerner, 1966) are well-suited. The latter may be a little easier to implement in shading language (due to the absence of variable-length arrays).

For the computation of the epsilon-delta bound, we use the following theorem:

Theorem 3.1 (cf. (Kranich, 2015, Theorem 2.1)). *Let $\mathcal{C}: f(x, y) = 0$ be a complex plane algebraic curve, where*

$$f(x, y) = \sum_{k=0}^n a_k(x) y^{n-k}$$

is a polynomial of degree n in y whose coefficients $a_k(x)$ are polynomials in x of the form

$$a_k(x) = \sum_{l=0}^{m_k} a_{kl} x^{m_k-l}.$$

Let $x_1 \in \mathbb{C}$ be a point in the complex plane at which neither the leading coefficient $a_0(x)$ nor the discriminant of $f(x, y)$ w.r.t. y vanish. Then for every $\varepsilon > 0$, we can algorithmically compute $\delta > 0$ such that

$$|y_j(x_1) - y_j(x_2)| < \varepsilon$$

for all holomorphic functions $y_j(x)$, $j = 1, 2, \dots, n$, which satisfy $f(x, y_j(x)) = 0$ in a neighbourhood of x_1 and for all x_2 with $|x_1 - x_2| < \delta$.

We obtain

$$\delta = \frac{\rho \left(\sqrt{(\rho Y - \varepsilon)^2 + 4\varepsilon M} - (\rho Y + \varepsilon) \right)}{2(M - \rho Y)}, \quad (4)$$

where

$$\begin{aligned} \rho &< \min\{|x_1 - x| : a_0(x) \cdot \Delta_y(f(x, y))(x) = 0\}, \\ Y &:= \max_j \left| \frac{f_x(x_1, y_j(x_1))}{f_y(x_1, y_j(x_1))} \right|, \quad M := 2 \max_k \left(\frac{\tilde{a}_k}{\tilde{a}_0} \right)^{\frac{1}{k}}, \\ \tilde{a}_0 &:= |a_{00}| \prod_{l=1}^{m_0} (|\bar{x}_l - x_1| - \rho) > 0, \quad \tilde{a}_k := \sum_{l=0}^{m_k} |a_{kl}| (|x_1| + |\rho|)^{n-l}, \end{aligned}$$

$\Delta_y(f(x, y))(x)$ denotes the y -discriminant of $f(x, y)$, and \bar{x}_l , $l = 1, 2, \dots, m_0$, are the zeros of $a_0(x)$.

Note that the computation is parallelizable since the epsilon-delta bound can be implemented as a function of x that depends on only a few constants derived from the coefficients of $f(x, y)$.

Instead of computing texture coordinates, which would depend on the range of $y(x)$ on the input domain, we generate the domain colouring procedurally on-the-fly. To that end, we use a variation of the enhanced phase portrait colour scheme of (Wegert, 2012, Section 2.5). The reference image is shown in Figure 4.1. We discuss the colour scheme in Subsection 4.1.

The main difference between the implementations in OpenGL and WebGL is how the common routines can be combined to realize Algorithm 2.1 and Algorithm 2.6.

3.1 An implementation in OpenGL

3.1.1 Implementation of Algorithm 2.1 in OpenGL

Our implementation of Algorithm 2.1 in OpenGL comprises three GLSL programs, for initialization, subdivision, and assembly of the Riemann surface mesh. We cache the output of each program using transform feedback and feed it back to the next program.

The initialization program consists only of a vertex shader, which operates on the vertices of the triangulated input domain. For every vertex x , we compute $y_k(x)$, $k = 1, 2, \dots, n$, and $\delta(x)$.

After initialization, we run the subdivision program. The program consists of a pass-through vertex shader and a geometry shader. The geometry shader operates on the triangles of the triangulated input domain or of its last subdivision, respectively. We have access to the values of x_j , $\delta(x_j)$, and $y_k(x_j)$, $k = 1, 2, \dots, n$, $j = 1, 2, 3$, at the vertices of each triangle $\Delta x_1 x_2 x_3$. We determine which edges of triangle $\Delta x_1 x_2 x_3$ are longer than the minimum of the $\delta(x_j)$ at their endpoints. In order to subdivide these edges, we compute their midpoints x , and $\delta(x)$ and $y_k(x)$, $k = 1, 2, \dots, n$, at the midpoints. We use the appropriate adaptive refine pattern of Figure 2.2 and output between one and four triangles for every input triangle. In doing so, we reuse previously computed values rather than recomputing them. We run the subdivision program iteratively until we reach the prescribed maximal subdivision depth.

The assembly program consists of a pass-through vertex shader and a geometry shader. The geometry shader operates on the triangles of the adaptively subdivided input domain. We again have access to the values of x_j , $\delta(x_j)$, and $y_k(x_j)$, $k = 1, 2, \dots, n$, $j = 1, 2, 3$, at the vertices of each triangle $\Delta x_1 x_2 x_3$. For every triangle $\Delta x_1 x_2 x_3$, we test whether one of its edges is longer than the minimum of the $\delta(x_j)$ at its endpoints. In this case, we discard the triangle. Otherwise, we determine the triangles of the Riemann surface mesh by proximity (see Algorithm 2.1, step 5) and output these n triangles.

We also cache the assembled Riemann surface mesh using transform feedback so that we can pass it as input to our implementation of the visualization algorithm (Algorithm 2.6).

3.1.2 Implementation of Algorithm 2.6 in OpenGL

Our implementation of Algorithm 2.6 in OpenGL consists of one GLSL program with a vertex and a fragment shader.

The vertex shader operates on the vertices of a Riemann surface mesh generated by our implementation of Algorithm 2.1. We apply height function $H: \mathbb{C} \rightarrow \mathbb{R}$ to map each (real) four-dimensional vertex

$$(\operatorname{Re} x, \operatorname{Im} x, \operatorname{Re} y(x), \operatorname{Im} y(x))$$

to a (real) three-dimensional vertex

$$(\operatorname{Re} x, \operatorname{Im} x, H(y(x))).$$

We homogenize the coordinates of this vertex and transform them using the model-view-projection matrix. We pass $y(x)$ as a varying variable to the fragment shader.

The fragment shader operates on the interpolated value of $y(x)$ at a fragment of a pixel of the output device. We compute the colour of $y(x)$ according to our domain colouring reference image.

3.1.3 Remarks

Using our implementation, the generation of a Riemann surface mesh takes little but noticeable time. The bottlenecks of the implementation are numerical root-finding and iterative subdivision. However, if we use transform feedback to cache the Riemann surface mesh and pass it to the implementation of the visualization algorithm, we obtain interactive performance.

Another advantage of using transform feedback to cache the Riemann surface mesh is that we can easily export the data. If we additionally compute texture coordinates and a high-resolution reference image, we can even print our visualization using a full colour 3D printer (see Figure 3.2).



Figure 3.2: 3D-printed models of domain-coloured Riemann surfaces of square root, folium of Descartes, and unit circle (clockwise). The merchandise coffee mug of DFG Collaborative Research Center TRR 109, “Discretization in Geometry and Dynamics”, is included in the picture as an indicator for the size of the models.

3.2 An implementation in WebGL

In order to support a wider range of devices, the WebGL API is much more limited than the OpenGL API. Particularly, in WebGL, geometry shaders and transform feedback are currently unavailable. (The WebGL 2 draft includes transform feedback and compute shaders.) Therefore our implementation in WebGL differs substantially from our implementation in OpenGL.

3.2.1 How to replace transform feedback

Instead of transform feedback, our implementation in WebGL uses floating point textures (specified in the `OES_texture_float` extension) and multiple render targets (specified in the `WEBGL_draw_buffers` extension). I do not claim originality of this approach. It is commonly used for running simulations on the GPU. The original idea may be due to (Crane et al., 2007). We number the vertices of every mesh consecutively and pass this number (index) to the vertex shaders along with the other attributes. In particular, vertices that are shared among several triangles must be duplicated and numbered separately. Hence, we assume that every triangle appears as three consecutive vertices in array buffer storage (triangle soup). We use floating point textures essentially as we

would arrays of floats, indexed by vertex number. We store values corresponding to the k -th vertex in the k -th pixel of a texture. We can store up to four floats per pixel of a floating point texture, namely one float each in the red, green, blue, and alpha channel. If we need to store more than four floats, we use multiple render targets which allows us to colour the same pixel of several textures simultaneously.

We want to store values we compute for a vertex in textures (‘transform’ in transform feedback). To that end, we bind the array buffers and draw the contents as points (as opposed to triangles). In the vertex shader, we compute the positions of the point with index k (in normalized device coordinates) so that it is rasterized as the k -th pixel of the render target textures. Recall that normalized device coordinates range in $[-1, 1]^3$. For example, if h and w denote the height and width of the textures in pixels, we assign to the point with index k the position

$$\left(\frac{2 \cdot (k \bmod w) + 1}{w} - 1, \frac{2 \cdot \lfloor k/w \rfloor + 1}{h} - 1, 0 \right).$$

In the fragment shader, we compute the values to be stored and assign them as output colours in a specific order (as we later want to retrieve them).

We want to read stored values for a vertex from textures (‘feedback’ in transform feedback). To that end, we bind the textures and an array buffer containing a range of vertex numbers (indices). We draw the contents of the array buffer as points or triangles (depending on whether we want to send the output to different textures or to the screen). In the vertex shader, we compute texture coordinates for the point with index k which allow us to lookup the k -th pixel from the textures. Recall that texture coordinates range in $[0, 1]^2$. For a texture of height h and width w , we compute the texture coordinates

$$\left(\frac{(k \bmod w) + 0.5}{w}, \frac{(k \bmod w) + 0.5}{h} \right).$$

Adding 0.5 in the numerators accounts for the fact that we want to obtain coordinates for the centre of a pixel in order to avoid interpolation with adjacent pixels. We pass the texture coordinates to the fragment shader, where we can use them to perform a texture lookup.

In order to access data of a whole triangle (as in geometry shaders), we can, in the vertex shader, determine the indices of the other vertices of the triangle. For example, the point with index k is part of the triangle whose vertices have indices

$$k - (k \bmod 3), \quad k - (k \bmod 3) + 1, \quad \text{and} \quad k - (k \bmod 3) + 2.$$

We compute normalized device coordinates or texture coordinates for all three indices and pass them to the fragment shader, together with the index of the triangle vertex currently under consideration.

3.2.2 How to replace geometry shaders

We replace the geometry shader of the subdivision program of our implementation in OpenGL using a variation of a method proposed by Boubekeur and Schlick (2008). The method works as follows: We precompute all adaptive refinement patterns up to a certain subdivision depth, in our case eight adaptive refinement patterns up to depth one (see Figure 2.2). We use barycentric coordinates to store the positions of the triangle vertices of each refinement pattern in an array buffer. Using array buffers of different lengths allows us to achieve variable-length output, as with geometry shaders. For every triangle of a coarse input mesh, we draw the triangles in the array buffer of the appropriate adaptive refinement pattern. We use the vertex positions of the input triangle (read from a texture or from uniform variables) and the barycentric coordinates of the triangles of the adaptive refinement pattern to compute the vertex positions of the output triangle.

We can combine this method with floating point texture and multiple render targets as outlined above, if we number the vertices of each adaptive refinement pattern consecutively and store those indices together with the barycentric coordinates. We pass an offset as a uniform variable to the vertex shader that needs to be added to the indices. We draw the adaptive refinement pattern and increment the offset by the number of vertices in the adaptive refinement pattern.

The geometry shader of the assembly program has fixed-length output. It generates exactly n triangles of the Riemann surface mesh per triangle of the (subdivided) input mesh. We can replace it with n invocations of a vertex shader, one for every sheet of the Riemann surface mesh. We pass the number of the current sheet to the vertex shader as a uniform variable.

3.2.3 Remarks

We cannot expect our WebGL implementation to reach the same performance as our OpenGL implementation. In the subdivision program, since we draw a different adaptive refinement pattern for every triangle of the input mesh, we lose parallelism. Consequently, subdivision in WebGL is much slower than its OpenGL counterpart. However, if we cache the assembled Riemann surface mesh (in textures) and pass it to our implementation of the visualization algorithm, we can still achieve interactive performance.

4 Examples

In this section, we discuss domain-coloured Riemann surface meshes for the complex square root function and for the folium of Descartes. Before that, let us explain our domain colouring reference image so that we can interpret the domain-coloured Riemann surface meshes.

4.1 Domain colouring reference image

Recall that the basic idea of domain colouring is the following: If we want to visualize a complex function

$$f: K \subset \mathbb{C} \rightarrow \mathbb{C},$$

we face the problem that its graph is real four-dimensional. However, we can visualize the behaviour of the function by colouring every point in its domain with the colour of the function value at that point in a reference image. The reference image is the domain colouring of the complex identity function.

Depending on what reference image we choose, we can read off various properties of a function from its domain colouring. For an overview of different colour schemes, we refer to (Poelke and Polthier, 2012; Wegert, 2012).

As our reference image, we use a variation of the enhanced phase portrait colour scheme of (Wegert, 2012, Section 2.5). The reference image is best described using polar coordinates

$$re^{i\varphi} = r(\cos \varphi + i \sin \varphi)$$

of a complex number with *modulus* $r > 0$ and *phase* $\varphi \in [0, 2\pi)$.

Firstly, we encode the phase at any point in the domain as the hue of its colour (in HSI colour space). In a square with side length 10 centred at the origin, we thus obtain the colour wheel shown in Figure 4.1a. As the phase changes from 0 to 2π , we obtain every colour of the rainbow. Positive real numbers, which have phase 0, are coloured in pure red. Negative real numbers, which have phase π , are coloured in cyan. Purely imaginary numbers do not have such distinctive colours. (This can be fixed using the NIST continuous phase mapping, which scales the phase piecewise linearly so that purely imaginary numbers with positive imaginary part become yellow and purely imaginary numbers with negative imaginary part become blue. See (NIST, 2014, <http://dlmf.nist.gov/help/vrml/aboutcolor#S2.SS2>). For simplicity, we do not follow this approach here.)

Secondly, we add contour lines of complex numbers of the same phase at integer multiples of 15 degrees (see Figure 4.1b). To that end, we change the intensity of the colour by multiplying it with a sawtooth function

$$0.7 + (1.0 - 0.7) \cdot (\varphi/(\pi/12) - \lfloor \varphi/(\pi/12) \rfloor).$$

Because phase corresponds to hue, the points of such a contour line are all of the same colour.

Finally, we add contour lines of complex numbers of the same modulus on a log-scale (see Figure 4.1c). To that end, we change the intensity of the colour by multiplying it with a sawtooth function

$$0.7 + (1.0 - 0.7) \cdot (\log(r)/(\pi/12) - \lfloor \log(r)/(\pi/12) \rfloor).$$

Note that the contour lines of phase and modulus intersect each other orthogonally. The scaling factor $1/(\pi/12)$ in the sawtooth function for the modulus

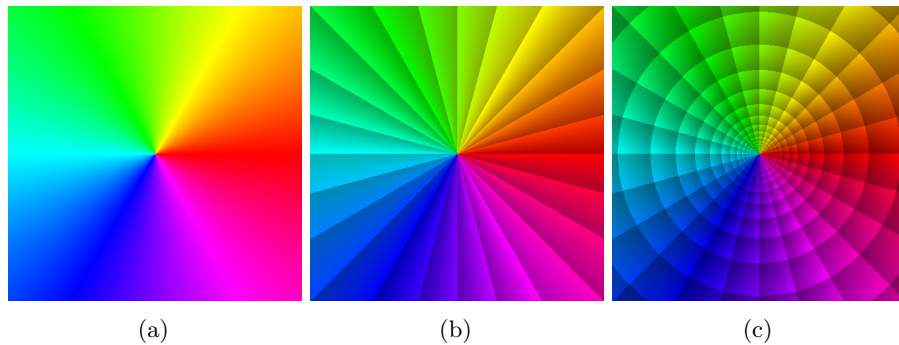


Figure 4.1: Composition of domain colouring reference image: If we (a) represent phase by hue, (b) add contour lines of phase and (c) add contour lines of modulus, we obtain our domain colouring reference image, a variation of the enhanced phase portrait colour scheme of (Wegert, 2012, Section 2.5).

contour lines deliberately matches the scaling factor used in the sawtooth function for the phase contour lines. Consequently, the regions enclosed by the contour lines of phase and modulus are squarish in appearance.

4.2 Complex square root

Recall the construction of a Riemann surface of the complex square root from Subsection 1.1 where we glued together its two branches at a branch cut along the negative real axis.

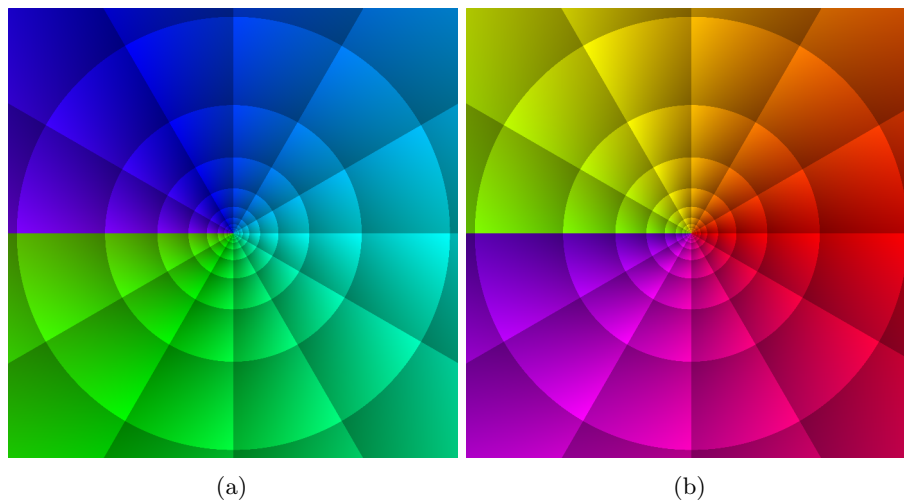


Figure 4.2: Domain colouring of the two sheets of the complex square root

The domain colouring of the two branches of the complex square root over a

square of side length 10 centred at the origin is shown in Figure 4.2.

On the sheet shown in Figure 4.2a, the complex square root takes values with negative real part (coloured green to blue). On the sheet shown in Figure 4.2b, it takes values with positive real part (coloured purple to yellow). (The sheet shown in Figure 4.2b corresponds to the principal branch of the complex square root.)

On both sheets, twelve contour lines of phase are visible, half as many as in the reference image. We can see that the phase of the complex square root function changes at half the angular velocity of its argument.

Moreover, the discontinuity at the branch cut along the negative real axis is clearly visible. We also see that there is a smooth transition between the second (third) quadrant of Figure 4.2a and the third (second) quadrant of Figure 4.2b.

If we cut the two sheets along the negative real axis and glue the upper side of the cut of one sheet to the lower side of the cut of the other sheet, and vice versa, we obtain a Riemann surface of the complex square root. The resulting Riemann surface, produced with Algorithm 2.1 and Algorithm 2.6 using real part as height function, is shown in Figure 4.3 (perspective) and Figure 4.4 (multiview orthogonal).

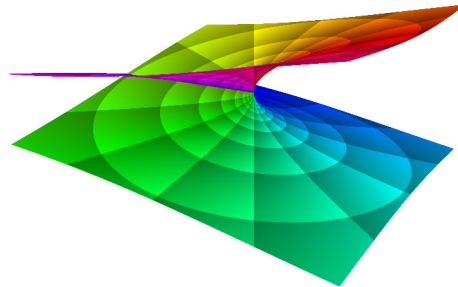


Figure 4.3: Domain-coloured Riemann surface of the complex square root in perspective projection

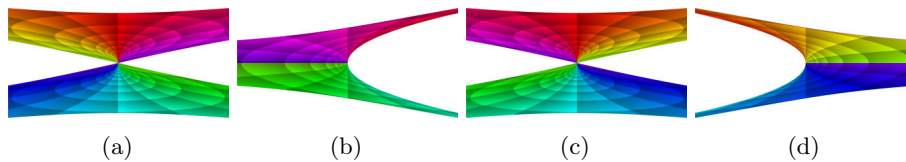


Figure 4.4: Domain-coloured Riemann surface of the complex square root in orthogonal projection from left, front, right, and back (from left to right)

Note that the self-intersection of the surface in Figure 4.3 is only an artefact of using a height function to map the Riemann surface mesh from real four-dimensional to real three-dimensional space. Evidently, the two values of the complex square root at each point of the self-intersection do not agree: they are coloured differently, in green and purple, respectively.

In Figure 4.4b, we see the parabola that the real parts of the y -values describe according to the equation $y^2 - x = 0$ when x takes values on the non-negative real axis.

4.3 Folium of Descartes

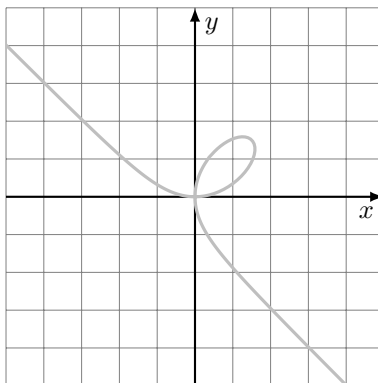


Figure 4.5: The folium of Descartes as a real plane algebraic curve

The folium of Descartes is a classical plane algebraic curve of order three,

$$\mathcal{C}: f(x, y) = x^3 + y^3 - 3xy = 0. \quad (5)$$

The cubic curve is nowadays called ‘folium’ after the leaf-shaped loop that it describes in the first quadrant of the real plane (see Figure 4.5). It is named in honour of the French geometer René Descartes (1596–1650), who was among the first mathematicians to introduce coordinates into geometry. Originally, the curve was called *fleur de jasmin* since Descartes and some of his contemporaries, who were working out the principles of dealing with negative and infinite coordinates, initially wrongly believed that the leaf-shaped loop repeated itself in the other quadrants and therefore resembled a jasmine flower (Loria, 1910, p. 53).

Figure 4.6 shows three domain-coloured sheets of the folium of Descartes over a square of side length 10 centred at the origin of the complex plane. We can generate these sheets by sorting the y -values that satisfy Equation 5 at every point x of the domain according to their real part. The sheet shown in Figure 4.6a uses the y -value with the smallest real part, the sheet shown in Figure 4.6b the y -value with the second-smallest real part, and the sheet shown in Figure 4.6c the y -value with the largest real part.

We see that the first sheet carries y -values with negative real part (coloured green to blue). At the centre of the second sheet, we identify a zero of order two, which we can recognize from the fact that the colours of the colour wheel used in our reference image wind around it twice in the same order as in the reference image. It is the node of the leaf-shaped loop. The third sheet carries y -values with positive real part (coloured purple to yellow).

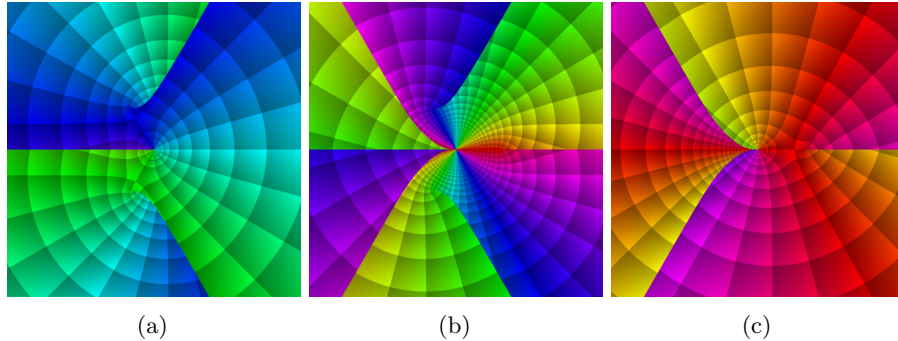


Figure 4.6: Domain colouring of three sheets of the folium of Descartes

There are three branch cuts (discontinuities of hue) on the first sheet, six on the second sheet and three on the third sheets. We can see how the sheets of the Riemann surface are connected to each other along the branch cuts: First and second sheet are connected at the branch cuts of the first sheet. Second and third sheet are connected at the branch cuts of the third sheet. First and third sheet are not connected directly with each other. (Imagine how much harder it would be to read this off from Equation 5.)

Apart from the branch cuts, the map from x to $y(x)$ is conformal (angle-preserving) on every sheet. We can see that the contour lines of phase and modulus intersect each other orthogonally on every sheet, as in our reference image.

If we cut the sheets along the branch cuts and glue them together correctly, we obtain a Riemann surface for the folium of Descartes.

The resulting Riemann surface, produced with Algorithm 2.1 and Algorithm 2.6 using real part as height function, is shown in Figure 4.7 (perspective) and Figure 4.8 (multiview orthogonal).

Again, the self-intersections of the surface in Figure 4.7 are only an artefact of using a height function to map the Riemann surface mesh from (real) four-dimensional to (real) three-dimensional space.

Figure 4.7 makes it obvious that cutting a Riemann surface into sheets by sorting y -values by real part may be the most straightforward but not necessarily the geometrically most appropriate method. Our Riemann surface of the folium of Descartes in large part appears to be composed of three copies of the complex plane (which looks like our reference image). Complications seem to arise only near the origin.

If we look closely at Figure 4.8b, we may see how we obtain the real folium of Descartes (as a real plane algebraic curve) as the intersection of our Riemann surface mesh with the $\text{Re } x$ - $\text{Re } y$ -plane. The leaf-shaped loop is clearly visible as a hole in our visualization. One of the ‘complex planes of which the Riemann surface is composed’ is so thin that it is barely visible from this perspective. It is almost asymptotic to the ‘wings’ of the folium of Descartes (as a real plane

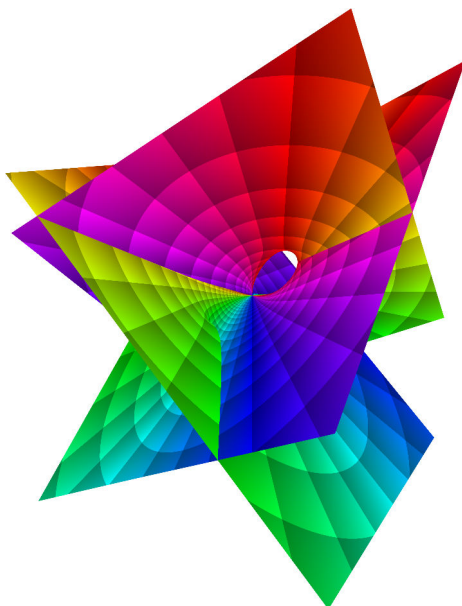


Figure 4.7: Domain-coloured Riemann surface of the folium of Descartes in perspective projection

algebraic curve) in the second and fourth quadrant of the real xy -plane.

Right below the centre of Figure 4.8c, we see two leaf-shaped loops in complex directions. Perhaps Descartes and his contemporaries were not entirely wrong after all to believe that the folium of Descartes has more than one leaf. Indeed, if we let $x' = e^{\pm i\pi/3}x$, we discover that in the $\text{Re } x'$ - $\text{Re } y$ -plane the curve describes a leaf-shaped loop, which is exactly half as high as that in the $\text{Re } x$ - $\text{Re } y$ -plane (this also holds for the ‘wings’) and rotated into a different quadrant (see Figure 4.9).

5 Conclusion

We have discussed algorithms for the generation of a Riemann surface mesh of a plane algebraic curve (Algorithm 2.1) and its visualization as a domain-coloured surface (Algorithm 2.6) and their implementation using OpenGL and WebGL. The WebGL implementation combines floating point textures, multiple render targets, and a method due to Boubekeur and Schlick (2008) to replace the use of transform feedback and geometry shaders of the OpenGL implementation. While the generation of the surface takes noticeable time in both implementations, the visualization of a cached Riemann surface mesh is possible with interactive performance. This allows us to visually explore otherwise almost unimaginable mathematical objects. Sometimes the visualization makes properties of the plane algebraic curves immediately apparent that may not so easily be read off from its equation. It is possible to turn these domain-coloured Riemann surface meshes

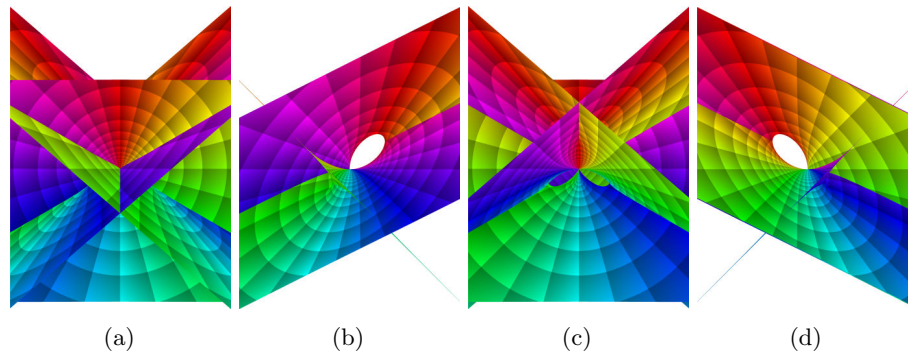


Figure 4.8: Domain-coloured Riemann surface of the folium of Descartes in orthogonal projection from left, front, right, and back (from left to right)

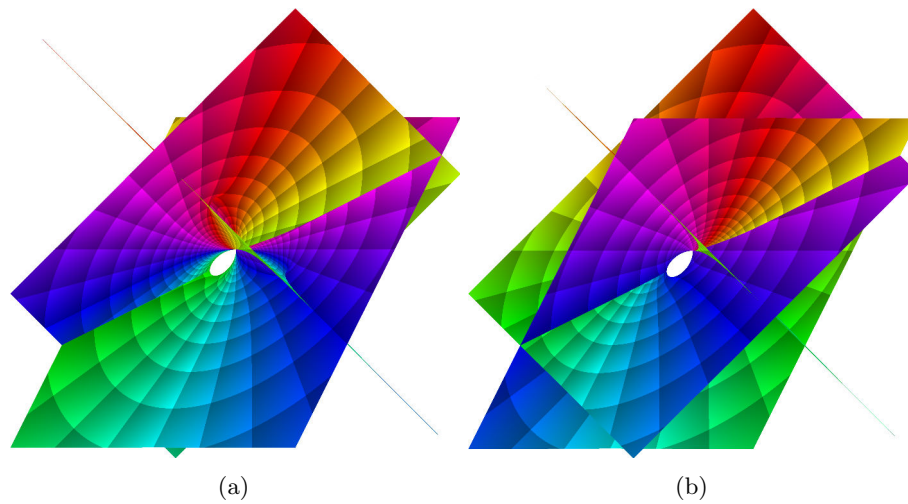


Figure 4.9: Leaf-shaped loops of the folium of Descartes in complex directions.

into physical models using a full colour 3D printer.

Funding

This research was supported by DFG Collaborative Research Center TRR 109, “Discretization in Geometry and Dynamics”.

References

- Boubekeur, Tamy and Christophe Schlick. 2008. *A Flexible Kernel for Adaptive Mesh Refinement on GPU*, Computer Graphics Forum **27**, no. 1, 102–113, DOI 10.1111/j.1467-8659.2007.01040.x.
- Crane, Keenan, Ignacio Llamas, and Sarah Tariq. 2007. *Real-Time Simulation and Rendering of 3D Fluids*, GPU gems 3 (Hubert Nguyen, ed.), Addison-Wesley, pp. 633–675.
- Durand, Émile. 1960. *Equations du type $F(x)$, racines d'un polynôme*, Solutions numériques des équations algébriques, vol. 1, Masson, Paris.
- Kerner, Immo O. 1966. *Ein Gesamtschrittverfahren zur Berechnung der Nullstellen von Polynomen*, Numerische Mathematik **8**, no. 3, 290–294, DOI 10.1007/BF02162564.
- Kranich, Stefan. 2012. *Real-time Visualization of Geometric Singularities*, Master's thesis, Technische Universität München.
- . 2015. *An epsilon-delta bound for plane algebraic curves and its use for certified homotopy continuation of systems of plane algebraic curves*, arXiv:1505.03432 [math.CV], available at <http://arxiv.org/abs/1505.03432>.
- Nieser, Matthias, Konstantin Poelke, and Konrad Polthier. 2010. *Automatic Generation of Riemann Surface Meshes*, Advances in Geometric Modeling and Processing (Bernard Mourrain, Scott Schaefer, and Guoliang Xu, eds.), Lecture Notes in Computer Science, vol. 6130, Springer, Berlin, pp. 161–178, DOI 10.1007/978-3-642-13411-1_11, (to appear in print).
- NIST (ed.) 2014. *NIST Digital Library of Mathematical Functions*. Release 1.0.9 of 2014-08-29. Online companion to (Olver et al., 2010). <http://dlmf.nist.gov>.
- Loria, Gino. 1910. *Spezielle algebraische und transzendente ebene Kurven: Theorie und Geschichte*, 2nd ed., translated by Schütte, Fritz, Vol. 1, Teubner, Leipzig (German).
- Olver, F. W. J., D. W. Lozier, R. F. Boisvert, and C. W. Clark (eds.) 2010. *NIST Handbook of Mathematical Functions*, Cambridge University Press, New York, NY. Print companion to (NIST, 2014).
- Poelke, Konstantin and Konrad Polthier. 2009. *Lifted Domain Coloring*, Computer Graphics Forum **28**, no. 3, 735–742, DOI 10.1111/j.1467-8659.2009.01479.x.
- . 2012. *Domain Coloring of Complex Functions: An Implementation-Oriented Introduction*, IEEE Computer Graphics and Applications **32**, no. 5, 90–97, DOI 10.1109/MCG.2012.100.
- Press, William H., Saul A. Teukolsky, William T. Vetterling, and Brian P. Flannery. 2007. *Numerical Recipes: The Art of Scientific Computing*, 3rd ed., Cambridge University Press, New York.
- Trott, Michael. 2008. *The Return of the Riemann Surface*, The Mathematica Journal **10**, no. 4, 626–656, DOI 10.3888/tmj.10.4-1.
- Wegert, Elias. 2012. *Visual Complex Functions: An Introduction with Phase Portraits*, Birkhäuser, Basel.
- Weierstraß, Karl. 1891. *Neuer Beweis des Satzes, dass jede ganze rationale Function einer Veränderlichen dargestellt werden kann als ein Product aus linearen Functionen derselben Veränderlichen*, Sitzungsberichte der Königlich Preußischen Akademie der Wissenschaften zu Berlin **2**, 1085–1101.